Synchrophasor Measurement Method Based on Cascaded Infinite Impulse Response and Dual Finite Impulse Response Filters

Boyu Zhao, Hao Liu, Tianshu Bi, and Sudi Xu

***Abstract*—High-precision synchronized measurement data with short measurement latency are required for applications of phasor measurement units (PMUs). This paper proposes a synchrophasor measurement method based on cascaded infinite impulse response (IIR) and dual finite impulse response (FIR) filters, meeting the M-class and P-class requirements in the IEC/IEEE 60255-118-1 standard. A low-group-delay IIR filter is designed to remove out-of-band interference components. Two FIR filters with different center frequencies are designed to filter out the fundamental negative frequency component and obtain synchrophasor estimates. The ratio of the amplitudes of the synchrophasor is used to calculate the frequency according to the one-to-one correspondence between the ratio of the amplitude frequency response of the FIR filters and the frequency. To shorten the response time introduced by IIR filter, a step identification and processing method based on the rate of change of frequency (RoCoF) is proposed and analyzed. The synchrophasor is accurately compensated based on the frequency and the frequency response of the IIR and FIR filters, achieving high-precision synchrophasor and frequency estimates with short measurement latency. Simulation and experiment tests demonstrate that the proposed method is superior to existing methods and can provide synchronized measurement data for M-class PMU applications with short measurement latency.**

***Index Terms*—Synchrophasor measurement, frequency estimation, infinite impulse response filter, complex bandpass filter.**

I. Introduction

PHASOR measurement units (PMUs) have been widely deployed in power transmission and distribution networks to monitor their steady and dynamic behaviors [1]-[3]. Due to a significant increase in installed renewable energy capacity, power system stability problems have become more common, requiring the implementation of real-time online applications based on real-time synchronized measurement data such as state estimation, emergency control, and fault location [4]-[6]. Therefore, higher accuracy of synchrophasor and frequency measurements with shorter measurement latency are required.

The IEC/IEEE 60255-118-1 standard classifies PMUs into measurement (M-class) and protection (P-class) types based on the application scenarios [7]. The core of a PMU is the synchronized measurement algorithm. Although the M-class PMU algorithm has high measurement accuracy, it has a longer measurement latency. While the P-class PMU has a shorter measurement latency but a narrower measurement bandwidth and a higher sensitivity to harmonics and out-of-band inter-harmonic interference. Therefore, it is challenging to calculate high-precision synchrophasor and frequency with short measurement latency because of the constraints between measurement accuracy and latency.

Existing synchrophasor measurement methods can be divided into the frequency-domain and time-domain methods. The former includes windowed discrete Fourier transform (DFT) methods [7]-[10], interpolated discrete Fourier transform (Ip-DFT) methods [11]-[15], the Taylor weighted least squares (TWLSs) method and its enhancements [16]-[18], etc. The performance of the DFT method depends on the frequency characteristics of the window function, whose default rectangular window can perform notch suppression for harmonics in steady state. However, when the harmonic frequency shifts with the fundamental frequency, the suppression performance is substantially reduced. Moreover, the rectangular window is difficult to extract the dynamic modulation components because of its uneven passband. Therefore, window functions such as the Hanning and Blackman windows have been used successively [7], [8]. They have a narrower transition bandwidth and are able to suppress the fundamental negative frequency components and the harmonic components when frequency offset occurs. However, problems such as main lobe attenuation in the measured bandwidth exist, resulting in poor dynamic performance. A window function with a smoother main lobe is designed to improve the dynamic performance [9], [10] and obtain a complex bandpass filter by frequency shifting, enabling synchrophasor calculation. This method has good dynamic performance and is simple to calculate, but it generally requires 4 cycles and

Manuscript received: October 27, 2023; revised: December 23, 2023; accepted: February 20, 2024. Date of CrossCheck: February 20, 2024. Date of online publication: March 27, 2024.

This work was supported by the National Natural Science Foundation of China (No. 52377098).

B. Zhao, H. Liu (corresponding author), and T. Bi are with the State Key Laboratory of Alternate Electric Power System with Renewable Energy Sources, North China Electric Power University, Beijing 102206, China (e-mail: byzhao@ncepu.edu.cn; hliu@ncepu.edu.cn; tsbi@ncepu.edu.cn).

S. Xu is with the State Grid Jiangsu Electric Power Research Institute, Nanjing 210036, China (e-mail: xsd19940526@126.com).

DOI: 10.35833/MPCE.2023.000824

longer data window, resulting in long measurement latency.

Researchers have proposed the Ip-DFT and its improvements to suppress the spectral leakage of the DFT method [11]-[15]. The Ip-DFT method compares two adjacent DFT spectral lines and reverses the frequency with a constructor. This method can effectively suppress the spectral leakage of the DFT method and has good performance in steady state. The enhanced Ip-DFT (E-Ip-DFT) [11], multi-spectral line Ip-DFT [12], and iterative Ip-DFT [13], [14] have been proposed to improve the dynamic performance. However, these methods are mainly aimed at M-class PMUs, and the use of short windows will affect their performance. In addition, the dual complex bandpass filter method (2CBPF) has been proposed. Two flat-top complex bandpass filters with different center frequencies are used to suppress the negative frequency component and extract the dynamic phasor. The two phasors are compared to obtain an approximate linear function only related to the frequency. The frequency is estimated by quadratic function fitting [15]. This method has good static and dynamic performance and short measurement latency, but it cannot suppress the harmonics and out-of-band components with high amplitude because it is designed for P-class PMUs.

The TWLS and its enhancements are the extension of the DFT method, which can directly obtain the frequency and rate of change of frequency (RoCoF) estimates through the Taylor series [16]-[18]. However, the phasor calculation model must be adjusted to the frequency, which is sensitive to out-of-band interference (OOBI) [16].

Time-domain methods include the nonlinear least squares method [19], [20], Prony method [21], [22], and the matrix pencil method [23], etc. The nonlinear least squares method establishes fitting equations based on signal models and solves synchrophasor through the least squares method, which has long measurement accuracy. However, it requires a longer window length to ensure the fitting accuracy, and has high requirements for hardware computing performance and sampling rate. The Prony method and matrix pencil method construct a characteristic polynomial and characteristic matrix according to the autoregression and autocorrelation of the samples and calculate the eigenvalues to estimate the frequency of the signal, respectively. These methods have high measurement accuracy but are sensitive to noises and out-of-band components [23].

The infinite impulse response (IIR) filter is rarely used for synchrophasor measurements due to its nonlinear phase delay. A synchrophasor measurement method based on the Hilbert transform has been proposed, where the IIR filter is used to filter out all negative frequency components in the spectrum, and the frequency and synchrophasor are estimated using the Ip-DFT method [24], [25]. After obtaining the frequency, the amplitude and phase of the synchrophasor are compensated according to the frequency response of the IIR filter accurately. This method has good static and dynamic performance. However, it requires a sufficiently long window length to ensure a good performance of the Ip-DFT method.

To address the above problems, a synchrophasor measurement method based on cascaded IIR and dual FIR filters is proposed to provide synchronized measurement data for power system applications requiring short measurement latency and high measurement accuracy. The main contributions of this paper are as follows.

1) A bilateral low-pass IIR filter with low group delay is designed to filter out harmonics and OOBI components. The performance of different design methods for IIR filters is analyzed to achieve better dynamic measurement performance.

2) Dual FIR filters with different center frequencies are designed to filter out the negative frequency components and extract two synchrophasors with sampling values in one power cycle. Reconstruction and difference steps are used to suppress the long-term spectral leakage of negative frequency components.

3) Based on the extracted synchrophasors, real-time frequency is calculated using the ratio of the synchrophasors' amplitudes. And the synchrophasor is accurately adjusted based on the estimated frequency and the frequency responses of the IIR and FIR filters.

4) A step identification method based on the RoCoF is proposed to reduce the response time of the IIR filtering process, and its sensitivity to different step sizes is analyzed.

The rest of this paper is organized as follows. Section II describes the measurement method and framework. Section III presents the filter design and step identification. The performance evaluation is presented in Section IV. Section V summarizes this paper.

II. Measurement Method and Framework

A. Signal Model

The dynamic signal model of voltage and current considering harmonics and OOBI in the power system is expressed as:

$$x(t)=\sum_{i=0}^{m}\sqrt{2}\,X_i(t)\cos\left(2\pi f_i t+\varphi_i(t)\right)+w(t) \tag{1}$$

where i denotes the fundamental ($i=0$) and i^{th} harmonic or inter-harmonic ($i=1,2,\ldots,m$), and m is the number of harmonic and inter-harmonic components; $X_i(t)$ and $\varphi_i(t)$ are the amplitude and phase of the harmonic or out-of-band inter-harmonic components, respectively; f_i is the constant part of the harmonic or out-of-band inter-harmonic frequency; and $w(t)$ is the noise term.

If the noise term is ignored, (1) can be written in polar coordinates according to Euler's formula:

$$x(t)\approx\sum_{i=0}^{m}\left(\frac{\sqrt{2}}{2}X_i(t)\mathrm{e}^{\mathrm{j}(2\pi f_i t+\varphi_i(t))}+\frac{\sqrt{2}}{2}X_i(t)\mathrm{e}^{-\mathrm{j}(2\pi f_i t+\varphi_i(t))}\right)=\sum_{i=0}^{m}\left(x_i^{+}(t)+x_i^{-}(t)\right) \tag{2}$$

where $x_i^{+}(t)$ and $x_i^{-}(t)$ are the positive and negative frequency components of the i^{th} harmonic or inter-harmonic, respectively. The fundamental synchrophasor and frequency are estimated by extracting $x_0^{+}(t)$. Therefore, it is necessary to suppress $x_0^{-}(t)$, $x_i^{+}(t)$, and $x_i^{-}(t)$.

B. Framework

Based on the relatively mature design methods of FIR filter, the frequency measurement method 2CBPF with short measurement latency oriented to P-class PMU is presented [15]. However, FIR filters typically require a higher order to meet the requirements of the M-class PMU for filtering out OOBI, which leads to two problems: ① the frequency response of the dual FIR filters in the measurement band becomes more similar, and the ratio of the amplitude frequency response and frequency does not satisfy a one-to-one correspondence near 50 Hz, causing 2CBPF method to fail; ② the measurement latency and response time increase. In contrast, IIR filters can achieve the same out-of-band suppression performance at lower orders. Therefore, an IIR filter is applied in this paper to filter the OOBI components while ensuring sufficient out-of-band suppression ability and reducing the order of the FIR filters.

However, there are two main problems with IIR filters. First, their nonlinear phase delay can cause a distortion in the dynamic modulation components, making it difficult to eliminate the group delay using FIR filters that mark the timestamp in the middle of the window. It is necessary to compensate the synchrophasor accurately based on the frequency. Second, the IIR filter has a convergence process, resulting in a longer step response time than FIR methods.

In response to the nonlinear phase problem, this paper designs a low-group-delay IIR filter to enhance the dynamic performance and designs dual FIR filters with low orders to estimate the synchrophasor and frequency simultaneously, then compensates the amplitude and phase of the synchrophasor accurately based on the frequency. Due to flexible passband and stopband planning methods, the FIR filter can filter out the negative frequency components of the fundamental signal. In response to the convergence process after signal steps, this paper proposes a step identification and processing link based on RoCoF to ensure rapid convergence, as described in Section III.

The proposed method can suppress the OOBI and fundamental negative frequency components using a combination of IIR and FIR filters. The frequency domain diagram of the proposed method is shown in Fig. 1. First, a low-pass IIR filter is designed to filter $x_i^+(t)$ and $x_i^-(t)$. Second, the dual FIR filters with different center frequencies are designed to suppress the fundamental negative frequency components $x_0^-(t)$, extract $x_0^+(t)$, and obtain two synchrophasors to achieve frequency estimation and precise synchrophasor compensation.

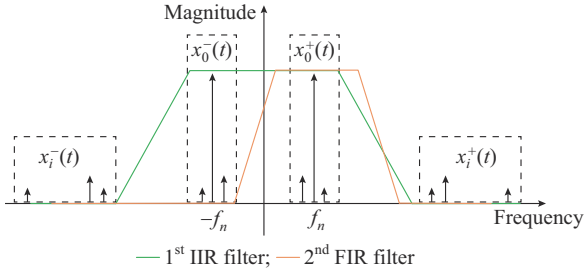

Fig. 1. Frequency domain diagram of proposed method.

We use the dual FIR filters with different center frequencies to extract $x_0^+(t)$ and suppress $x_0^-(t)$. For simplicity, the filtering process of one FIR filter is described, and the usage of the other filter is the same:

$$\begin{aligned}\boldsymbol{X}(t_k)=&\left[\sum_{n=-N}^{N}h(n)\bar{x}\left(t_k+\frac{n}{f_s}\right)\right]\mathrm{e}^{-\mathrm{j}2\pi f_0 t_k}\approx\\&H_{IIR}(f_0)H_{FIR}(f_0)x_0^+(t_k)\mathrm{e}^{-\mathrm{j}2\pi f_0 t_k}\approx\\&\left|H_{IIR}(f_0)\right|\left|H_{FIR}(f_0)\right|X_0(t_k)\mathrm{e}^{\mathrm{j}(\varphi_0(t_k)+\varphi_{IIR}(f_0)+\varphi_{FIR}(f_0))}\end{aligned}\tag{3}$$

where $\boldsymbol{X}(t_k)$ is the estimated synchrophasor at time t_k, whose amplitude and phase are $X(t_k)$ and $\varphi(t_k)$, respectively; $h(n)$ is the coefficient of the FIR filter, with an order of $2N+1$ (N is a positive integer); $\bar{x}(\cdot)$ is the signal sequence filtered by the IIR filter; f_s is the sampling frequency; $H_{IIR}(f_0)$ and $H_{FIR}(f_0)$ are the frequency responses of the IIR and FIR filters, respectively; and $X_0(t_k)$ and $\varphi_0(t_k)$ are the real amplitude and phase of the synchrophasor at time t_k, respectively.

Due to the limitation of the filter order, the amplitude frequency response of the designed IIR and FIR filters is not completely flat within the measurement band, and the phase frequency response of the IIR filter is not linear. Therefore, the amplitude and phase of the initially calculated $\boldsymbol{X}(t_k)$ must be corrected based on the frequency. The signal frequency is estimated using the 2CBPF method [15] to reduce the measurement latency of the synchrophasor and frequency.

The 2CBPF calculates the frequency according to the one-to-one correspondence between the ratio of the amplitude frequency response of the dual FIR filters and the frequency. The frequency calculation is as follows:

$$R_H=\frac{\left|H_1(f_0)\right|}{\left|H_2(f_0)\right|}=G(f_0)\tag{4}$$

$$R_X=\frac{\left|\boldsymbol{X}_1(t_k)\right|}{\left|\boldsymbol{X}_2(t_k)\right|}\approx\frac{\left|H_{IIR}(f_0)\right|\left|H_1(f_0)\right|X_0(t_k)}{\left|H_{IIR}(f_0)\right|\left|H_2(f_0)\right|X_0(t_k)}=\frac{\left|H_1(f_0)\right|}{\left|H_2(f_0)\right|}=R_H\tag{5}$$

$$\hat{f}_0=G^{-1}(R_X)\tag{6}$$

where R_H is the ratio of the frequency responses $H_1(f_0)$ and $H_2(f_0)$ of the dual FIR bandpass filters h_1 and h_2; $\boldsymbol{X}_1(t_k)$ and $\boldsymbol{X}_2(t_k)$ are the synchrophasors calculated by the dual FIR filters; $\hat{f}_0$ is the estimated frequency; and R_X is the ratio of their amplitudes.

Based on the frequency response of the IIR filter and the FIR filter, $\boldsymbol{X}(t_k)$ can be compensated to obtain the accurate synchrophasor $\boldsymbol{X}_0(t_k)$:

$$\boldsymbol{X}_0(t_k)=\frac{\boldsymbol{X}(t_k)}{H_{IIR}(f_m)H_{FIR}(f_m)}\mathrm{e}^{\mathrm{j}(\varphi(t_k)-\varphi_{IIR}(f_m)-\varphi_{FIR}(f_m))}\tag{7}$$

where $H_{IIR}(f_m)$, $\varphi_{IIR}(f_m)$, $H_{FIR}(f_m)$, and $\varphi_{FIR}(f_m)$ are the amplitude frequency responses and phase frequency responses of the IIR and FIR filters at the measurement frequency f_m, respectively.

The RoCoF is calculated from the backward difference of the frequency:

$$rf(k)=\frac{\hat{f}_0(k)-\hat{f}_0(k-M)}{M}F_c\tag{8}$$

where $rf(k)$ is the estimated RoCoF; F_c is the calculation frequency; and M is the calculation interval.

Due to the difficulty in completely filtering out the negative frequency component of the fundamental wave when the order of the FIR filter is low, increasing the filter order can lead to a higher similarity between the dual FIR filters in the measurement band, resulting in a nonlinear relationship between their frequency response ratio and the frequency. Therefore, we reconstruct the negative frequency component of the fundamental wave and subtract it from the original signal to suppress the negative frequency component of the fundamental wave. The flowchart of the proposed method is shown in Fig. 2.

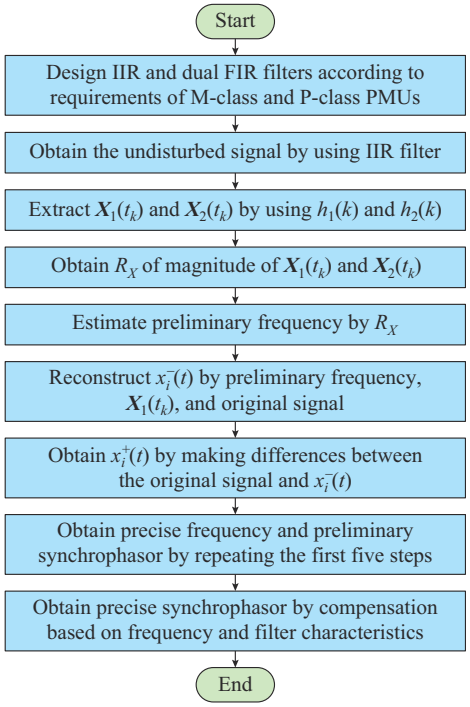

Fig. 2. Flowchart of proposed method.

III. Filter Design and Step Identification

A. Out-of-band Component Suppression: IIR Filter

A low-pass IIR filter is used to suppress the OOBI. The IIR filter is designed using the Butterworth, Chebyshev type I and type II, ellipse, and the minimum P-norm methods with the same design requirements. The amplitude frequency response and phase frequency response of the IIR filters designed with different methods are shown in Figs. 3 and 4, respectively. The filters designed using the Butterworth method have a smaller passband ripple, but their group delay is high, and their transition band attenuation is slow, resulting in a slow response speed and low resistance to OOBI. The filter designed using the Chebyshev type I and ellipse methods has fast transition band attenuation, but the passband ripple is large, resulting in poor dynamic performance. Although the passband ripple and group delay of the filter designed using the Chebyshev type II method are small, they are greater than those obtained from the minimum P-norm method. Thus, the dynamic performance and response speed are slightly inferior to that of the minimum P-norm method.

Therefore, the minimum P-norm method is used in this paper to design the IIR filter using the filter design module in MATLAB 2018b. The parameters of the IIR filter are listed in Table I, and its frequency response is shown in Fig. 3. The IIR filter has a passband ripple of less than 0.02 dB, an out-of-band gain of less than −80 dB, and a maximum group delay of 13.88 ms within the measurement band.

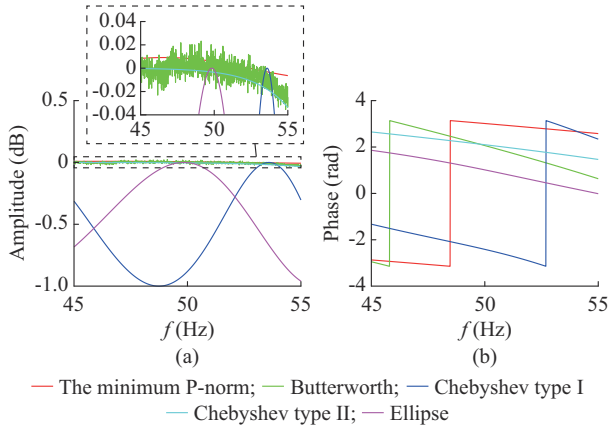

Fig. 3. Amplitude frequency response and phase frequency response of IIR filters designed using different methods. (a) Amplitude frequency response. (b) Phase frequency response.

TABLE I
Parameters of IIR Filter

Parameter	Value
Sampling frequency	1000 Hz
Reporting frequency	100 Hz
Section	2
Order	8
Passband range	[0, 60]Hz
Passband ripple	≤0.02 dB
Out-of-band gain	≤−80 dB
Group delay (45-50 Hz)	12.75 ms
Group delay (50-55 Hz)	13.88 ms

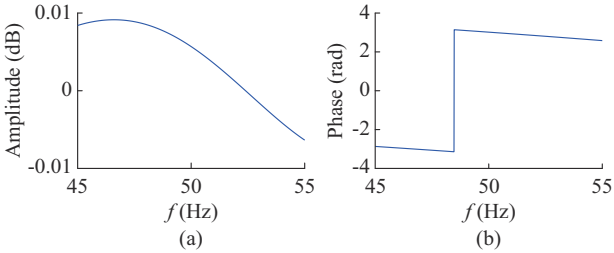

Fig. 4. Amplitude frequency response and phase frequency response of designed IIR filter. (a) Amplitude frequency response. (b) Phase frequency response.

B. Negative Frequency Component Suppression: Dual FIR Filters

Bandpass FIR filter design methods can be divided into direct and indirect methods. Direct methods include the least

square-based class design method, iterative reweighted least square method, and other methods based on optimization criteria. Indirect methods design low-pass filter firstly and obtain a bandpass filter by the frequency shift. The low-pass filter design methods include window function method, frequency sampling method, and the equiripple method, etc. Since the low-pass filter design method is more mature and simple [26], we use it to design a low-pass filter and perform frequency shifting to construct a bandpass filter.

The Hanning, Blackman, Hamming, and other window functions have fast sidelobe attenuation and complete suppression of all harmonics. However, their passband attenuation is generally fast, resulting in low-dynamic performance, and the harmonic suppression performance is low when the fundamental frequency deviates from the rated value [10]. The frequency sampling method can effectively suppress harmonic components when the filter order is an integer multiple of half a cycle; however, it has poor dynamic performance. For the same order, the equiripple method has the smallest ripple in the passband, and the band weight of the filter can be customized to suppress the negative frequency component [15].

Therefore, we use the equiripple method to design the low-pass filters and obtain two complex bandpass filters by frequency shifting. The parameters of designed FIR filters are listed in Table II, and their amplitude frequency response and the ratio of dual FIR filters R_H are shown in Fig. 5. The center frequencies of the dual FIR filters are 45 Hz and 55 Hz, and the gains at the negative frequency component of the fundamental wave are lower than −65 dB and −70 dB, respectively.

TABLE II
PARAMETERS OF DESIGNED FIR FILTERS

Parameter	Filter 1	Filter 2
Sampling frequency	1000 Hz	1000 Hz
Reporting frequency	100 Hz	100 Hz
Order	21	21
Center frequency	45 Hz	55 Hz
Passband range	[40, 50]Hz	[50, 60]Hz
Passband ripple	≤0.03 dB	≤0.03 dB
Gain at negative frequency component	≤−65 dB	≤−70 dB

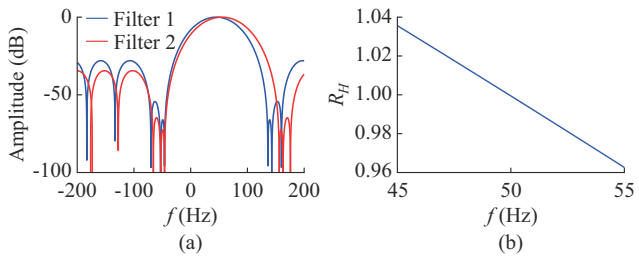

Fig. 5. Amplitude frequency response and ratio of dual FIR filters. (a) Amplitude frequency response. (b) Ratio of dual FIR filter.

It should be noted that we do not use two FIR filters for negative frequency component suppression. Instead, each FIR filter independently suppresses the negative frequency components and extracts the fundamental synchrophasor. The main differences in the design of dual FIR filters are the center frequency and passband, which lead to different amplitude frequency responses within the measurement band.

However, the test has shown that the estimation accuracy of the method does not meet the requirements of the M-class PMU standard. The reason is that the fundamental negative frequency component is equivalent to an interference component with an amplitude of 100% of the fundamental positive frequency component, and its amplitude is much higher than the out-of-band components. Therefore, the FIR filter cannot completely filter out this component.

Therefore, we reconstruct the negative frequency component of the fundamental wave and determine the difference to suppress the negative frequency component of the fundamental wave. It is achieved using the r^{th} calculation of phasor and frequency and subtracting the result from the original sampling values to obtain a value sequence, containing only the fundamental positive frequency component:

$$x_r^-(t)=\frac{\sqrt{2}}{2}X_r e^{-j(2\pi f_r t+\varphi_r)} \tag{9}$$

$$x_r^+(t)=x_{r-1}(t)-x_r^-(t) \tag{10}$$

where $x_r^-(t)$ and $x_r^+(t)$ are the reconstructed values of the r^{th} calculation of the fundamental negative and positive frequency components, respectively; X_r, φ_r, and f_r are the amplitude, phase, and frequency of the r^{th} calculation of the fundamental synchrophasor, respectively; and $x_{r-1}(t)$ is the $(r-1)^{\text{th}}$ reconstruction signal sequence.

The $(r+1)^{\text{th}}$ synchrophasor and frequency estimation values can be obtained by filtering $x_r^+(t)$ and comparing the amplitudes. Since the FIR filter has already removed the negative frequency component of the fundamental wave, only one iteration of the reconstruction and subtraction is required to achieve good suppression of the negative frequency component at relatively low-computational complexity.

C. Step Identification and Processing

When a step occurs in the electrical quantity, IIR filtering requires time to converge, increasing the step response time of the proposed method. Therefore, based on the sensitivity of the 2CBPF method to the non-continuous signal, we propose a step identification method of electrical quantities based on the RoCoF. The flowchart of the proposed step identification and processing method is shown in Fig. 6. Firstly, the initial frequency is calculated by the IIR and dual FIR filters. Secondly, the frequency value is subtracted from that of the previous calculation time to determine whether the frequency variation exceeds the threshold. If the threshold is not exceeded, no step has occurred, and the final estimated value is obtained through compensation according to filter characteristics. If the threshold is exceeded, the IIR filtering process is terminated, and the proposed method is transformed into the 2CBPF to achieve a fast step response.

The tests related to the frequency variation in the IEC/IEEE 60255-118-1 standard include the frequency ramp test and the phase modulation (PM) test, with RoCoF of 1 Hz/s and 5π Hz/s, respectively. The maximum RoCoF in the se-

vere fault event of the South Australia power grid in 2016 was 6 Hz/s. Therefore, we use a frequency difference threshold of 0.2 Hz, corresponding to RoCoF of 20 Hz/s with a reporting rate of 100 Hz to identify the electrical quantity steps. These settings are appropriate for most non-step dynamic scenarios.

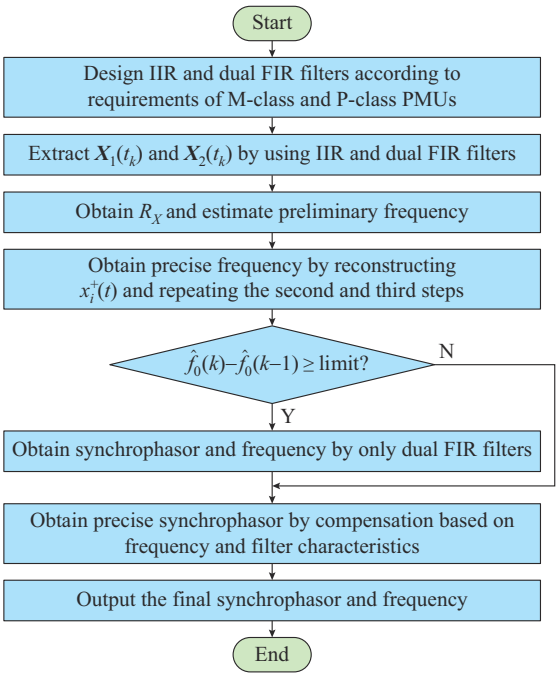

Fig. 6. Flowchart of step identification and processing method.

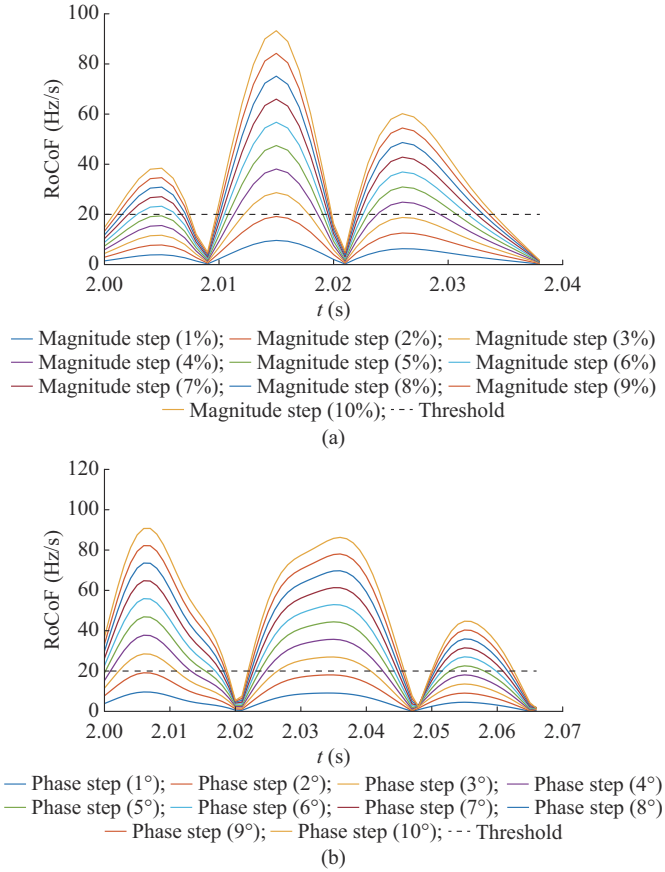

Fig. 7. Absolute value of RoCoF calculations under magnitude and phase steps. (a) Magnitude step. (b) Phase step.

Although the magnitude step specified in the IEC/IEEE 60255-118-1 standard is 10% times the amplitude value of fundamental wave and the phase step is 10°, the step in the actual power system may be lower than this value. Therefore, this paper analyzes the sensitivity of the proposed method to smaller range steps. The absolute values of RoCoF calculations under magnitude and phase steps are shown in Fig. 7. The step occurs at 2 s, and the sampling frequency and calculation frequency are both set to be 1000 Hz to simulate signal steps that may occur at any sampling time.

Figure 7 indicates that after a step occurs, regardless of its magnitude, the RoCoF will exhibit three significant peaks. If the calculated RoCoF values near these peaks consistently exceed the set threshold, the step is considered to occur. In practical devices, to conserve hardware resources, the calculation frequency is often set lower, such as 100 Hz, which is one-tenth of the calculation frequency shown in Fig. 7. Therefore, the proposed method can accurately identify a step as long as the RoCoF values for 10 consecutive calculation points exceed the threshold, irrespective of when the step occurs within the sampling period. Consequently, the proposed method can accurately detect step signals with magnitude steps greater than or equal to 5% and phase steps greater than or equal to 3°. Signal distortion is always present when a step occurs in the actual power system, causing more drastic changes in RoCoF compared with those shown in Fig. 7. Therefore, the sensitivity of the proposed method in the actual power system will be further enhanced.

IV. Performance Evaluation

A. Test Conditions

We compare the proposed method (denoted as M1) with the method recommended by the IEC/IEEE 60255-118-1 standard [7] (denoted as M2), the 2CBPF method [15] (denoted as M3), and the iterative Ip-DFT method [13] (denoted as M4) through simulation tests. M2 is the windowed DFT method, which has been widely used for synchrophasor and frequency estimation in commercial PMUs. M3 is the 2CBPF method deployed in synchronized measurement device for control (SMC) (P-class PMU) for estimating the frequency and RoCoF. M4 is an improved Ip-DFT method with good static and dynamic performance. These methods have been implemented in the device, and their performance has been verified in actual power systems.

The sampling frequency of the proposed method in the simulation and experimental tests is 1000 Hz, the reporting rate is 100 Hz, and the window length is 1 cycle (corresponding to a 20 ms time window length in a 50 Hz power system). The timestamp of the proposed method is 4 ms before the window to eliminate the group delay of the IIR and dual FIR filters. Therefore, the synchrophasor measurement latency is 24 ms. The data window lengths of M2, M3, and M4 are set to be 4, 2, and 4 cycles, respectively, with a sampling rate of 10000 Hz. Their timestamps are in the middle of the time window, the synchrophasor measurement laten-

cies are 40 ms, 20 ms, and 40 ms, respectively, and the frequency measurement latencies are 50 ms, 20 ms, and 40 ms, respectively.

The static and dynamic test conditions for the M-class PMU in the IEC/IEEE 60255-118-1 standard are listed in Table III, where k_x is the amplitude modulation (AM) depth, k_p is the PM depth, R_f is the RoCoF in the frequency ramp test, k_{sx} is the amplitude step size, and k_{sp} is the phase step size. The fundamental component has a frequency offset of 0.5 Hz in the harmonic impact and dynamic modulation tests. In addition, 60 dB of Gaussian white noise is added to the simulation test signals to address the errors introduced by low-pass filtering, digital-to-analog conversion, and other processes during signal sampling and processing.

TABLE III
STATIC AND DYNAMIC TEST CONDITIONS

Test type	Parameter
Frequency offset	$X_m = 57.73$ V, 45 Hz $\le f_0 \le 55$ Hz
Harmonic distortion	$X_m = 57.73$ V, $f_0 = 50.5$ Hz, harmonic magnitude is $0.1X_m$, frequency is up to the 9th order
OOBI	$X_m = 57.73$ V, $f_0 = 55$ Hz, inter-harmonic magnitude is $0.1X_m$, frequency is 105 Hz to 145 Hz with an interval of 5 Hz
Dynamic modulation	$X_m = 57.73$ V, $f_0 = 50.5$ Hz, $f_m = 0.2$ Hz - 5 Hz, AM: $k_x = 0.1$, $k_p = 0$, PM: $k_x = 0$, $k_p = 0.1$
Frequency ramp	$X_m = 57.73$ V, $f_0 = 48$ Hz-52 Hz, $R_f = \pm 1$ Hz/s
Amplitude step	$k_{sx} = \pm 0.1X_m$, $k_{sp} = 0$
Phase step	$k_{sx} = 0$, $k_{sp} = \pm\pi/18$

B. Simulation

The test signals are generated by MATLAB at a sampling frequency of 1 kHz. Because the signal models are known in advance, the true values of the frequency and RoCoF can be obtained. The proposed method and the comparison methods are used to estimate the synchrophasor, frequency, and RoCoF of the static and dynamic signals. The estimation errors are obtained by comparing the measured and true values.

1) Off-nominal Tests

Off-nominal tests are used to assess the measurement accuracy of the methods during the frequency offset. Figure 8 shows the total vector error (TVE) and frequency error (FE) of the proposed methods and the comparison methods for different frequency offsets. In Table IV, the maximum TVE, maximum FE, and maximum RoCoF error (RFE) are listed. Std represents the maximum error of the M-class PMU standard. The trend of the RFE is similar to that of FE; therefore, it is not represented in Fig. 8.

Figure 8 shows that when the frequency offset is large, the TVE of M2 is significantly higher than that of the other methods, whereas the TVEs of M1, M3, and M4 are not significantly affected. The maximum FEs of M2, M3, and M4 exceed the standard requirements. M2 is a DFT method based on the Hamming window. When the fundamental frequency shifts, its ability to suppress negative frequency components decreases, significantly increasing the TVE and FE. M3 is typically used for protection and control application scenarios. Thus, it has good dynamic performance in the range of [48, 52]Hz. However, when the frequency offset exceeds 2 Hz, its measurement accuracy does not meet the requirements of the M-class PMU standards. M4 has the minimum TVE due to the iterative process, but its FE is relatively large due to the long-range spectral leakage of the negative frequency component. M1 initially suppresses the negative frequency component of the fundamental component due to the FIR filter and further suppresses it by reconstruction and modification. Therefore, the frequency measurement accuracy is significantly higher than that of the comparison methods.

TABLE IV
THE MAXIMUM MEASUREMENT ERROR OBTAINED FROM OFF-NOMINAL TESTS

Method	TVE (%)	FE (Hz)	RFE (Hz/s)
Std	1.0000	0.0050	0.1000
M1	0.0100	0.0011	0.0520
M2	0.1300	0.0120	0.6900
M3	0.0170	0.0067	0.2600
M4	0.0055	0.0084	0.0028

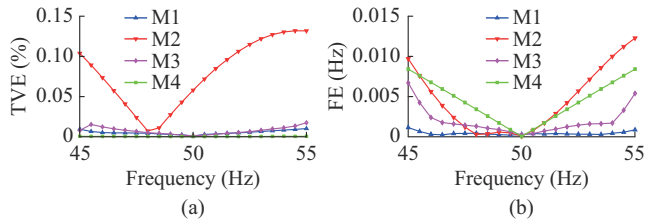

Fig. 8. TVE and FE of different methods in off-nominal tests. (a) TVE. (b) FE.

2) Harmonic Distortion Tests

Harmonic distortion tests are used to evaluate the ability of the method to suppress harmonic interference. The TVE and FE of different methods in the harmonic distortion tests are shown in Fig. 9, and the maximum measurement error is listed in Table V. The proposed method has good suppression ability for harmonics due to the pre-filtering of IIR filter of the out-of-band components. M2 has a larger TVE because it does not have a module for suppressing harmonics. M3 is used for P-class PMU and considers scenarios where the harmonic amplitude is 0.01 times the fundamental amplitude. When it increases to 0.1 times the fundamental amplitude, the ability of M3 to suppress second-order harmonics does not meet the standard requirements. M4 adopts the iterative Ip-DFT method; thus, its accuracy is significantly higher than that of M2, which is equivalent to the accuracy of the proposed method.

3) OOBI Tests

OOBI tests are used to assess the ability of method to suppress OOBI. The results of the TVE and FE methods obtained from the OOBI tests are shown in Fig. 10, and the maximum measurement error is listed in Table VI. M2 is limited by the filter order, and its Hamming window sidelobe attenuation reaches its limit, preventing it from completely filtering out the interference components.

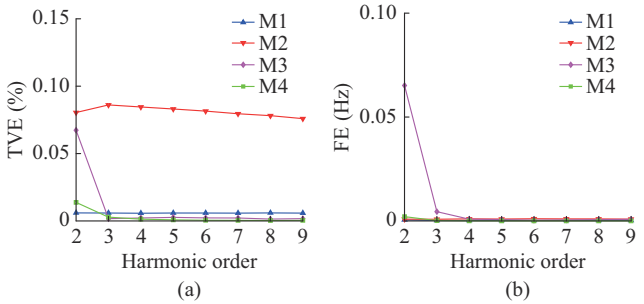

Fig. 9. TVE and FE of different methods in harmonic distortion tests. (a) TVE. (b) FE.

TABLE V
THE MAXIMUM MEASUREMENT ERRORS OBTAINED FROM HARMONIC DISTORTION TESTS

Method	TVE (%)	FE (Hz)	RFE (Hz/s)
Std	1.0000	0.0250	-
M1	0.0067	0.0027	0.013
M2	0.0860	0.0010	0.013
M3	0.0670	0.0650	0.410
M4	0.0140	0.0021	0.014

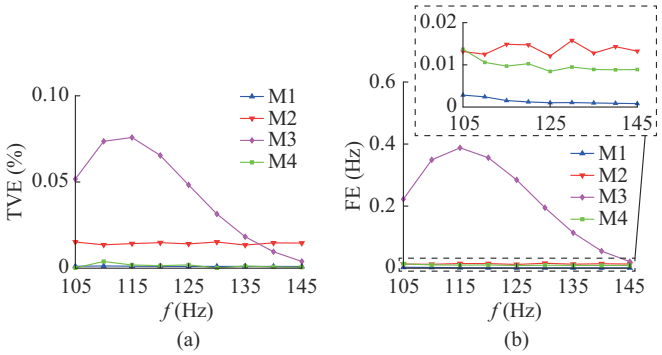

Fig. 10. TVE and FE of different methods in OOBI tests. (a) TVE. (b) FE.

TABLE VI
THE MAXIMUM MEASUREMENT ERRORS OBTAINED FROM OOBI TESTS

Method	TVE (%)	FE (Hz)	RFE (Hz/s)
Std	1.300	0.0100	-
M1	0.013	0.0028	0.140
M2	0.150	0.0160	0.310
M3	0.760	0.3900	7.300
M4	0.039	0.0140	0.170

Therefore, the accuracy of M2 is slightly lower than that of M1 and M4. M3 is suitable for P-class PMUs and does not consider OOBI. As the difference between the interference component frequency and harmonic frequency increases, the calculation error increases. When the out-of-band component amplitude is 0.1 times the fundamental wave amplitude, the frequency measurement error does not meet the standard requirements. The accuracy of M4 is significantly higher than that of M2, meeting the standard requirements. M1 uses an IIR filter to pre-filter the out-of-band components, resulting in good suppression of out-of-band components at all frequencies and the highest measurement accuracy.

4) AM Tests

The AM test is used to evaluate the dynamic performance of the methods. The TVE and FE of the different methods in AM tests are shown in Fig. 11. The measurement errors of the methods increase with the modulation frequency. The maximum measurement errors are listed in Table VII. M1 eliminates the partial group delay by shifting the timestamp forward; thus, it has the minimum TVE. However, due to the nonlinear phase of the IIR filter and the solving frequency based on the amplitude ratio, the frequency measurement accuracy of M1 is significantly affected by AM. Due to the high passband attenuation of the filters, the phasor measurement accuracy of M2 and M4 is lower than that of M1. M3 has the smallest TVE due to its smoother passband. Due to the nonlinear phase of IIR, the frequency and RoCoF estimation errors of M1 (0.022 Hz, 0.68 Hz/s) are slightly higher than those of the comparison methods but lower than one-tenth of the standard requirement (0.3 Hz, 14 Hz/s).

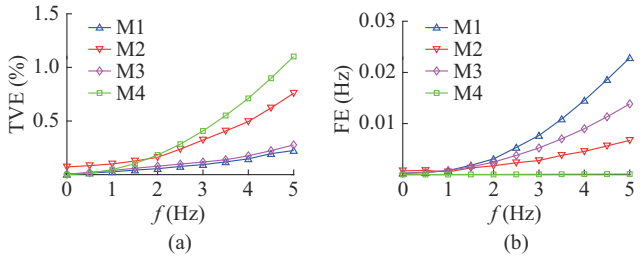

Fig. 11. TVE and FE of different methods in AM tests. (a) TVE. (b) FE.

TABLE VII
THE MAXIMUM MEASUREMENT ERRORS OBTAINED FROM AM TESTS

Method	TVE (%)	FE (Hz)	RFE (Hz/s)
Std	3.00	0.30000	14.0000
M1	0.22	0.02200	0.6800
M2	0.76	0.00670	0.2000
M3	0.28	0.01400	0.4000
M4	1.10	0.00013	0.0052

5) PM Tests

The TVE and FE of different methods in the PM test are shown in Fig. 12. The measurement errors of each method increase with the modulation frequency. The maximum measurement errors are listed in Table VIII. Since M1 cannot extract all dynamic modulation components from the nonlinear phase, its TVE is relatively large. However, the frequency measurement accuracy of M1 is not affected by PM because its frequency solution is based on the amplitude rather than the phase. M2 and M4 have larger TVEs and FEs due to the uneven passband. M3 has the smallest TVE and FE due to its relatively flat passband and low order, resulting in smaller dynamic changes in the phase of the signal in the data window.

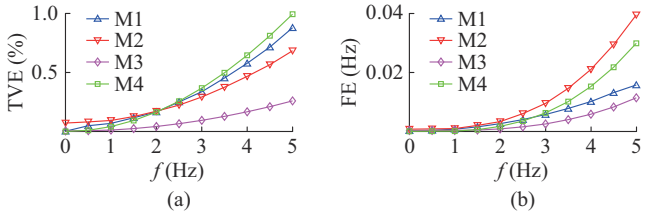

Fig. 12. TVE and FE of different methods in PM tests. (a) TVE. (b) FE.

TABLE VIII
THE MAXIMUM MEASUREMENT ERRORS OBTAINED FROM PM TESTS

Method	TVE (%)	FE (Hz)	RFE (Hz/s)
Std	3.00	0.300	14.00
M1	0.88	0.016	0.62
M2	0.68	0.040	1.50
M3	0.26	0.011	4.90
M4	0.99	0.030	1.20

6) Frequency Ramp Tests

Frequency ramp tests are used to simulate an out-of-step power system and evaluate the ability of the methods to suppress the negative frequency component of the fundamental component during the frequency offset and the flatness of the filter in the measurement frequency band. The maximum measurement errors of different methods in the frequency ramp tests are listed in Table IX. M1 has the smallest TVE and FE due to its smoother passband and additional suppression of negative frequency components.

TABLE IX
THE MAXIMUM MEASUREMENT ERRORS OBTAINED FROM FREQUENCY RAMP TESTS

Method	TVE (%)	FE (Hz)	RFE (Hz/s)
Std	1.000	0.0100	0.2000
M1	0.021	0.0020	0.0260
M2	0.210	0.0100	0.4700
M3	0.300	0.0080	0.0370
M4	0.067	0.0068	0.0042

Due to the uneven passband of M2, the measurement error is relatively large. M3 has the shortest data window length and a relatively flat passband, but it does not perform processing on the negative frequency component during the frequency offset, resulting in low accuracy in phasor and frequency measurements. The iterative interpolation process of M4 increases the ability of DFT method to track the time-varying phase and frequency, resulting in significantly higher measurement accuracy than M2.

7) Step Tests

Step tests are used to simulate sudden changes in electrical quantities caused by switching operations and faults in the power system and test the response speed of the methods. The maximum measurement errors obtained from amplitude step tests and phase step tests are listed in Table X and Table XI, respectively. Due to the effective identification of the amplitude and phase steps by the proposed step identification method, M1 switches to M2 when a step is detected, resulting in a faster response. Therefore, the response time is slightly longer than that of M3. M2 and M4 use four cycles of windows, resulting in longer phasor and frequency response time. Since M2 calculates the frequency based on the phase difference, and M4 directly obtains the frequency from the Ip-DFT method, the frequency of M2 and RoCoF response time are longer than those of M4.

TABLE X
THE MAXIMUM MEASUREMENT ERRORS OBTAINED FROM AMPLITUDE STEP TESTS

Method	TVE (ms)	FE (ms)	RFE (ms)
Std	140	280	280
M1	29	42	46
M2	30	70	100
M3	19	36	42
M4	39	61	73

TABLE XI
THE MAXIMUM MEASUREMENT ERRORS OBTAINED FROM PHASE STEP TESTS

Method	TVE (ms)	FE (ms)	RFE (ms)
Std	140	280	280
M1	31	42	46
M2	37	70	120
M3	24	39	42
M4	47	67	77

8) Noise Tests

In the noise tests, Gaussian white noise is added to the static signal to test the anti-noise performance of the methods. The TVE and FE of different methods in noise tests are shown in Fig. 13, and the maximum measurement errors are listed in Table XII. SNR is short for signal-noise-ration of the signal.

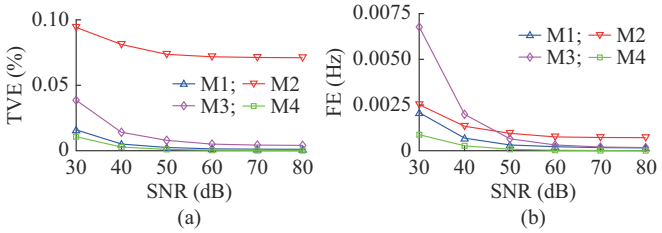

Fig. 13. TVE and FE of different methods in noise tests. (a) TVE. (b) FE.

TABLE XII
THE MAXIMUM MEASUREMENT ERRORS OBTAINED FROM NOISE TESTS

Method	TVE (%)	FE (Hz)	RFE (Hz/s)
Std	1.000	0.00500	0.100
M1	0.016	0.00210	0.180
M2	0.094	0.00250	0.170
M3	0.039	0.00680	0.560
M4	0.011	0.00087	0.064

Since the IEC/IEEE 60255-118-1 standard does not have noise test requirements, a static test is used to obtain Std. As shown in Fig. 13, M2 cannot completely filter out the negative frequency component of the fundamental component, and M3 has insufficient stopband attenuation, resulting in larger TVEs and FEs. M1 and M4 have good noise suppression capabilities due to their better noise filtering performance.

9) Computational Complexity Analysis

The main computational complexity of the methods is shown in Table XIII. The number of sampling points in a cycle is K ($K=20$ at the sampling rate of 1000 Hz). M1 is more computationally intensive than M3 due to the presence of IIR filtering process although it uses only one cycle sampling points. M2 is simple to compute and less computationally intensive. The high accuracy of M4 relies on the high sampling rate, which is most computationally intensive due to the high number of samples used and the presence of iterative computational process.

TABLE XIII
COMPUTATIONAL COMPLEXITY OF DIFFERENT METHODS

Method	Sampling points used	Multiplication	Addition
M1	K	$18K$	$18K$
M2	$4K$	$16K$	$8K$
M3	$2K$	$8K$	$8K$
M4	$40K$	$320K$	$320K$

To study the simulation time consumption, the proposed method is tested using a laptop with a processor of AMD R7 4800 (base frequency of 2.9 GHz) and 16 GB of RAM, with the software environment of MATLAB R2020a. 600 simulations of M1 are performed, and the maximum simulation time of a single simulation is less than 3×10^{-5} s, which is much less than the maximum computation time limit of 0.01 s (at the reporting rate of 100 Hz), indicating that M1 can meet the demand of real-time computation.

10) Summary of Performance Results

In summary, M2 is more sensitive to the frequency offset and PM, and the frequency and RoCoF have the longest response time in the amplitude and phase angle steps. M3 has good performance for dynamic modulation and has the fastest response speed during the steps. However, its ability to suppress low-order harmonics, inter-harmonics, and noise is insufficient, resulting in lower frequency measurement accuracy than M1. M4 has the most accurate phasor estimation results when frequency offset occurs and the most accurate frequency estimation during the AM test. It is not sensitive to OOBI and noise, but its frequency estimation is susceptible to the frequency offset, and it has a relatively long response time. Although M1 has significant estimation errors under dynamic modulation, it is not sensitive to the frequency offset. In addition, it has strong resistance to OOBI and noise and a strong tracking ability when the frequency changes linearly, exhibiting more balanced static and dynamic performances.

C. Experiments

A PMU prototype consisting of a synchronized timing module (NI 9467), voltage acquisition board (NI 9244), and real-time embedded controller (NI Crio-9039) is built, and M1 is implemented using LABVIEW language.

The hardware schematic diagram of the PMU prototype is shown in Fig. A1 of Appendix A. The synchrophasor and frequency estimation includes three parts: signal sampling, phasor and frequency estimation, and data uploading. The signal sampling is conducted by controlling NI 9467 (global position system (GPS) module) and NI 9244 (voltage acquisition module) using a field-programmable gate array (FPGA) (NI Crio-9039). The pulse per second is received from NI 9467, and a digital phase-locked loop (DPLL) is used to generate a sampling clock synchronized with GPS to NI 9244 for synchronized voltage signal sampling. Subsequently, the sample values from NI 9244 are encapsulated, and a data queue with timestamps is generated to match with the real-time module of NI Crio-9039.

The phasor estimation and data communication functions are included in the real-time module of NI Crio-9039, including receiving sampling data queues, estimating the phasor and frequency, outputting measurement results, generating data frames, and uploading them.

A PMU prototype test platform is created to evaluate the measurement accuracy of the PMU prototype, as shown in Fig. A2 of Appendix A.

The high-precision signal source OMICRON 256 plus is calibrated [9], [10], and the signal generator and PMU prototype are synchronized with the GPS receiver. Static and dynamic test signals in Table III are sent to the PMU prototype. The estimation errors are calculated by comparing the estimated results of the PMU prototype with the actual phasor and frequency values. The experimental results of M1 are listed in Table XIV.

TABLE XIV
EXPERIMENTAL RESULTS OF M1

Test type	TVE (%)		FE (Hz)		REE (Hz/s)	
	Std	M1	Std	M1	Std	M1
Off-nominal	1.0	0.0150	0.005	0.0019	0.1	0.054
Harmonic	1.0	0.0081	0.025	0.0029		0.012
OOBI	1.3	0.0210	0.010	0.0052		0.320
AM	3.0	0.2500	0.300	0.0270	14.0	0.780
PM	3.0	0.8900	0.300	0.0160	14.0	0.680
Frequency ramp	1.0	0.0260	0.010	0.0033	0.2	0.042

The accuracy of the phasor, frequency, and RoCoF is lower than that obtained from the simulations. For example, the TVE and FE of M1 are 0.010% and 0.0011 Hz in the simulation tests and 0.015% and 0.0019 Hz in the prototype tests, respectively, in the frequency offset tests. The reason is that the test system has uncertainty, and the PMU hardware has synchronization and sampling errors. The maximum estimation errors of the PMU prototype in all tests are smaller than the standard limit. Therefore, M1 can accurately estimate the fundamental synchrophasor and frequency.

V. Conclusion

This paper proposes a synchrophasor measurement method based on cascaded IIR and dual FIR filters. Synchronized measurement data provided for power system applications require short measurement latency and high accuracy measurement. The IIR filter can remove the harmonic and other OOBI, which is not considered in M3. The negative frequency component of the fundamental component is filtered by the dual FIR filters initially and subsequently eliminated by reconstruction and refinement. A step identification method based on RoCoF is proposed to avoiding convergence issues caused by IIR filter, and its sensitivity to different step sizes is analyzed. The latency of the proposed method is 24 ms, close to the requirements of the P-class PMU and shorter than most M-class PMUs. Simulations and experiments show that the synchrophasor accuracy is at least 3 times higher than the M-class standard requirements, and a minimum response time around 40 ms is achieved when magnitude or phase steps. Future studies will focus on the correction and repair of synchrophasor and frequency during transient step.

Appendix A

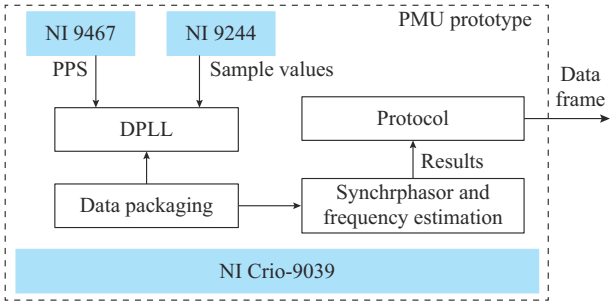

Fig. A1. Hardware schematic diagram of PMU prototype.

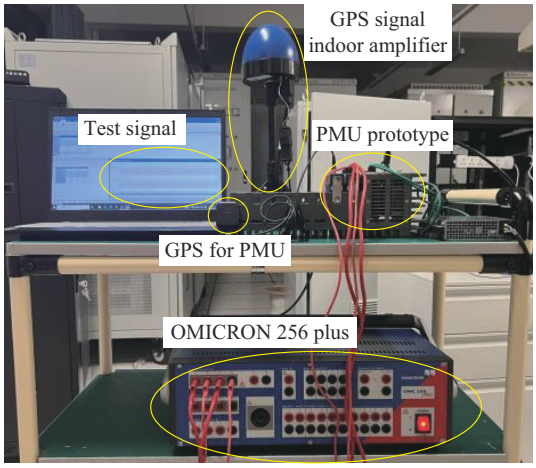

Fig. A2. PMU prototype test platform.

References

[1] J. G. Philip, J. Jung, and A. Onen, "Empirical wavelet transform based method for identification and analysis of sub-synchronous oscillation modes using PMU data," *Journal of Modern Power Systems and Clean Energy*, vol. 12, no. 1, pp. 34-40, Jan. 2024.

[2] M. U. Usman and M. O. Faruque, "Applications of synchrophasor technologies in power systems," *Journal of Modern Power Systems and Clean Energy*, vol. 7, no. 2, pp. 211-226, Mar. 2019.

[3] Y. Liu, L. Zhan, Y. Zhang *et al.*, "Wide-area-measurement system development at the distribution level: an FNET/GridEye example," *IEEE Transactions on Power Delivery*, vol. 31, no. 2, pp. 721-731, Apr. 2016.

[4] J. D. L. Ree, V. Centeno, J. S. Thorp *et al.*, "Synchronized phasor measurement applications in power systems," *IEEE Transactions on Smart Grid*, vol. 1, no. 1, pp. 20-27, Jun. 2010.

[5] Z. Liu, P. Li, C. Wang *et al.*, "Robust state estimation of active distribution networks with multi-source measurements," *Journal of Modern Power Systems and Clean Energy*, vol. 11, no. 5, pp. 1540-1552, Sept. 2023.

[6] A. N. Sheta, G. M. Abdulsalam, A. A. Eladl, "Online tracking of fault location in distribution systems based on PMUs data and iterative support detection," *International Journal of Electrical Power & Energy Systems*, vol. 128, pp. 1-10, Jun. 2021.

[7] *IEEE/IEC International Standard – Measuring Relays and Protection Equipment – Part 118-1: Synchrophasor for Power System Measurements*, IEC/IEEE 60255-118-1, 2018.

[8] A. G. Phadke and J. S. Thorp, *Synchronized Phasor Measurements and Their Applications*. New York: Springer-Verlag, 2008.

[9] S. Xu, H. Liu, T. Bi *et al.*, "A high-accuracy phasor estimation algorithm for PMU calibration and its hardware implementation," *IEEE Transactions on Smart Grid*, vol. 11, no. 4, pp. 3372-3383, Jul. 2020.

[10] S. Xu, H. Liu, and T. Bi, "A general design method for phasor estimation in different applications," *IEEE Transactions on Smart Grid*, vol. 12 no. 3, pp. 2307-2319, May 2021.

[11] P. Romano and M. Paolone, "Enhanced interpolated-DFT for synchrophasor estimation in FPGAs: theory, implementation, and validation of a PMU prototype," *IEEE Transactions on Instrumentation and Measurement*, vol. 63, no. 12, pp. 2824-2836, Dec. 2014.

[12] K. Wang, S. Liu, L. Wang *et al.*, "Novel interpolation method of multi-DFT-Bins for frequency estimation of signal with parameter step change," *IEEE Transactions on Instrumentation and Measurement*, vol. 71, pp. 1-14, Jan. 2022.

[13] A. Derviškadić, P. Romano, and M. Paolone, "Iterative-interpolated DFT for synchrophasor estimation: a single algorithm for P- and M-class compliant PMUs," *IEEE Transactions on Instrumentation and Measurement*, vol. 67, no. 3, pp. 547-558, Mar. 2018.

[14] K. Wang, H. Wen, G. Li *et al.*, "Iterative two-point interpolated DFT algorithm for accurate frequency estimation," *IEEE Transactions on Power Delivery*, vol. 37, no. 3, pp. 1671-1681, Jun. 2022.

[15] S. Xu, H. Liu, and T. Bi, "A novel frequency estimation method based on complex bandpass filters for P-class PMUs with short reporting latency," *IEEE Transactions on Power Delivery*, vol. 36, no. 6, pp. 3318-3328, Dec. 2021.

[16] D. Belega, D. Fontanelli, and D. Petri, "Low-complexity least-squares dynamic synchrophasor estimation based on the discrete Fourier transform," *IEEE Transactions on Instrumentation and Measurement*, vol. 64, no. 12, pp. 3284-3296, Dec. 2015.

[17] L. Fu, S. Xiong, C. Pan *et al.*, "A multiple frequency taylor model-based dynamic synchrophasor estimation algorithm," *IEEE Transactions on Smart Grid*, vol. 10, no. 6, pp. 6870-6882, Nov. 2019.

[18] Ž. Zečević and B. Krstajić, "Dynamic harmonic phasor estimation by adaptive taylor-based bandpass filter," *IEEE Transactions on Instrumentation and Measurement*, vol. 70, pp. 1-9, Aug. 2021.

[19] H. Liu, S. Xu, T. Bi *et al.*, "Non-linear fitting-based phasor measurement method for PMU calibrator," *International Journal of Electrical Power & Energy Systems*, vol. 106, pp. 585-597, Mar. 2019.

[20] J. Wold and F. Wilches-Bernal, "Enhanced nonlinear least squares for power system frequency estimation with phase jump immunity," *International Journal of Electrical Power & Energy Systems*, vol. 129, pp. 1-8, Jul. 2021.

[21] S. Ando, "Frequency-domain Prony method for autoregressive model identification and sinusoidal parameter estimation," *IEEE Transactions on Signal Processing*, vol. 68, pp. 3461-3470, Jun. 2020.

[22] J. Khodaparast, O. B. Fosso, and M. Molinas, "Phasor estimation by EMD-assisted Prony," *IEEE Transactions on Power Delivery*, vol. 37, no. 6, pp. 4736-4748, Dec. 2022.

[23] J. Li, H. Liu, T. Bi *et al.*, "Second-order matrix pencil-based phasor measurement algorithm for P-class PMUs," *IET Generation Transmission & Distribution*, vol. 14, no. 19, pp. 3953-3961, Oct. 2020.

[24] G. Frigo, A. Derviškadić, and M. Paolone, "Reduced leakage synchrophasor estimation: Hilbert transform plus interpolated DFT," *IEEE Transactions on Instrumentation and Measurement*, vol. 68, no. 10, pp. 3468-3483, Oct. 2019.

[25] A. Derviškadić, G. Frigo, and M. Paolone, "Beyond phasors: modeling of power system signals using the Hilbert transform," *IEEE Transactions on Power Systems*, vol. 35, no. 4, pp. 2971-2980, Jul. 2020.
[26] P. Cheng, *Digital Signal Processing Course*. Beijing: Tsinghua University Press, 2013.

Boyu Zhao received the B.S. degree in electrical engineering and automation from North China Electric Power University, Beijing, China, in 2021, where he is currently pursuing the Ph. D. degree in electrical engineering. His research interests include efficient characterization and computational methods for electrical quantities in power systems.

Hao Liu received the Ph.D. degree in electrical engineering from North China Electric Power University, Beijing, China, in 2015, where he is currently an Associate Professor. His research interests include testing, calibration, and applications for synchronized measurement technique.

Tianshu Bi received the Ph.D. degree in electrical and electronic engineering from the University of Hong Kong, Hong Kong, China, in 2002. She is currently a Professor at North China Electric Power University, Beijing, China. Her research interests include power system protection and control, and synchrophasor measurement technique and its application.

Sudi Xu received the Ph.D. degree in electrical engineering from North China Electric Power University, Beijing, China, in 2022. He is currently with the State Grid Jiangsu Electric Power Research Institute, Nanjing, China. His research interests include synchrophasor estimation and phasor measurement unit calibration techniques.